

2D material platform for overcoming the amplitude-phase tradeoff in ring modulators

Ipshita Datta¹, Andres Gil-Molina¹, Sang Hoon Chae^{2,3}, James Hone² and Michal Lipson¹

¹Department of Electrical Engineering, Columbia University, New York, New York 10027, USA

²Department of Mechanical Engineering, Columbia University, New York, New York 10027, USA

³School of Electrical & Electronic Engineering, School of Materials Science and Engineering, Nanyang Technological University, Singapore 639798, Singapore

Corresponding Author – ml3745@columbia.edu

Abstract – Compact, high-speed electro-optic phase modulators play a vital role in various large-scale applications including phased arrays, quantum and neural networks, and optical communication links. Conventional phase modulators suffer from a fundamental tradeoff between device length and optical loss that limits their scaling capabilities. High-finesse ring resonators have been traditionally used as compact intensity modulators, but their use for phase modulation have been limited due to the high insertion loss associated with the phase change. Here, we show that high-finesse resonators can achieve a strong phase change with low insertion loss by simultaneous modulation of the real and imaginary parts of the refractive index, to the same extent. To implement this strategy, we utilize a hybrid platform that combines a low-loss SiN ring resonator with electro-absorptive graphene (Gr) and electro-refractive WSe₂. We achieve a phase modulation efficiency ($V_{\pi/2} \cdot L_{\pi/2}$) of 0.045 V · cm with an insertion loss ($IL_{\pi/2}$) of 4.7 dB for a phase change of $\pi/2$ radians, in a 25 μm long Gr-Al₂O₃-WSe₂ capacitor embedded on a SiN ring of 50 μm radius. We find that our Gr-Al₂O₃-WSe₂ capacitor can support an electro-optic bandwidth of 14.9 ± 0.1 GHz. We further show that the $V_{\pi/2} \cdot L_{\pi/2}$ of our SiN-2D platform is at least an order of magnitude lower than that of electro-optic phase modulators based on silicon, III-V on silicon, graphene on silicon and lithium niobate. This SiN-2D hybrid platform provides the impetus to design compact and high-speed reconfigurable circuits with graphene and transition metal dichalcogenide (TMD) monolayers that can enable large-scale photonic systems.

Introduction

Conventional photonic materials used in phase modulators, typically exhibit low index change ranging from 0.01 % in lithium niobate (LiNbO₃) to 0.1 % for semiconductors such as silicon and III-V (see supplementary section I). This low index change requires hundreds of microns of interaction length for a phase change of π radians¹⁻²⁵. In high-speed intensity modulators^{26,16,27,28}, it is possible to achieve effective modulation in a compact form-factor by using high-finesse ring resonators to increase the interaction length and enhance modulation depth.

However, high-finesse ring resonators have not been successfully implemented for phase modulation, due to the associated large insertion loss and undesired intensity modulation. This loss arises due to the effect of a large mismatch between the change in real (Δn) and imaginary part (Δk) of the index for conventional materials used for phase modulation in ring resonators. As an example, in figure 1a, we show the transmission (T_{Ring}) and phase response (φ_T) of a ring resonator embedded with an active material that undergoes a strong change in index i.e. $\frac{\Delta n}{\Delta k} \sim -20$, typically observed in silicon. The ring is critically-coupled with a loaded quality factor (Q_L) of $\sim 20,000$ and undergoes a Δn of -6×10^{-4} RIU (refractive index units), as is commonly reported in silicon-based electro-refractive modulators²⁸⁻³⁰. The index change in the active material induces a shift in the resonance wavelength of the ring response. At a probe wavelength of λ_p , the cavity experiences a phase change of $\sim \pi/2$ radians that is accompanied by an unacceptably high insertion loss of 9 dB. Previous demonstrations have leveraged low-finesse over-coupled ring resonators for phase modulation^{31,32}. However, these modulators require high index change and therefore, must rely on the thermo-optic effect which is an inherently slow and power-hungry mechanism.

Here, we demonstrate an alternative strategy for achieving strong phase change in resonators with low insertion loss and minimal transmission variation. This strategy requires that the ratio of the index change (Δn) to the loss change (Δk) has to be approximately equal to unity, i.e. $\frac{\Delta n}{\Delta k} \sim 1$ (see Supplementary section II). In figure 1b, we show the T_{Ring} and φ_T at the output of a ring resonator utilizing an embedded hybrid active material with $\frac{\Delta n}{\Delta k} \sim 1$, operating near the critically-coupled regime with an initial Q_L of ~ 20000 and a Δn of -6×10^{-4} RIU. In this case, Δn causes resonance detuning, while Δk results in an enhancement of the coupling between the ring resonator and the bus waveguide. One can see from the phase profile in figure 1b, that these effects transform the φ_T from a gradual phase variation near the critically-coupled condition to a strongly dispersive phase profile in the over-coupled regime with a detuning of the resonance wavelength. When probed at λ_p , one can achieve a strong phase change of $\sim \pi$ radians with an insertion loss as low as 4.5 dB. However, no known dielectric material exhibits a $\frac{\Delta n}{\Delta k} \sim 1$ at near-infrared (NIR) wavelengths.

To enable simultaneous tuning of both the real and imaginary part of the effective index, we utilize a capacitive stack of monolayer tungsten disulphide (WSe₂) and graphene (Gr) integrated in a low-loss dielectric ring resonator. Figure 1c shows a schematic of the structure consisting of the stack of the 2D materials (Gr-Al₂O₃-WSe₂) embedded on a 1300 nm wide \times 330 nm high silicon nitride (SiN) waveguide covered with 180 ± 15 nm of planarized silicon dioxide (SiO₂). We tune the electro-optic properties of the 2D materials by applying a voltage across the dielectric alumina (Al₂O₃) that is sandwiched between the two monolayers. Our design benefits from the electro-absorptive properties of Gr³⁴⁻³⁶ (which effectively tunes the ring-bus coupling) and the electro-refractive properties of monolayer transition metal-dichalcogenide (TMD) such as WSe₂³⁷ (which

changes the resonance wavelength). The ratio between the real (Δn_{eff}) and imaginary part (Δk_{eff}) of the effective index in a composite SiN-2D waveguide, is determined by the relative overlap of the propagating mode with each of the 2D monolayers. The overlap with Gr influences both the initial propagation loss and Δk_{eff} , while the overlap with the monolayer WSe₂ predominantly contributes to the Δn_{eff} . The bare SiN resonator with a radius of 50 μm , is fabricated with an intrinsic quality factor (Q_0) of $\sim 112,000$ (i.e. $\alpha_{\text{SiN}} \sim 5.98 \pm 0.38$ dB/cm). The ring resonator is designed to achieve critical-coupling with a Q_L of $\sim 20,870$ at 8 V, by embedding a 40 μm long Gr-Al₂O₃-WSe₂ capacitor in the ring with a ring-bus gap of 350 nm (hereafter, referred to as device I). The SiO₂-clad SiN waveguides were fabricated using standard techniques, and then planarized to permit the mechanical transfer and lithographic patterning of the Gr-Al₂O₃-WSe₂ capacitor with metal contacts in the SiN ring resonator. We estimate a linear induced charge density of $(0.85 \pm 0.03) \times 10^{12}$ cm⁻² per volt on both the monolayers, based on the thickness (45 nm) and the extracted dielectric permittivity of Al₂O₃ (6.9 ± 0.2) (see Methods).

Results

We measure a continuous phase change ($\Delta\varphi_T$) of $(0.46 \pm 0.05) \pi$ radians with an insertion loss (IL) of 4.78 ± 0.40 dB. This $\Delta\varphi_T$ is accompanied with a transmission variation (ΔT_{Ring}) of 4.37 ± 0.70 dB for an applied voltage swing from 6 V to 18 V. In figure 2a, we show using blue square markers, the $\Delta\varphi_T$ (top panel) and the ΔT_{Ring} (bottom panel) for different voltages applied across the Gr-Al₂O₃-WSe₂ capacitor. We probe the $\Delta\varphi_T$ and ΔT_{Ring} at a wavelength detuning λ_p , where the phase change is maximum while ensuring a low IL and ΔT_{Ring} . In this case, λ_p is 0.03 nm blue-detuned from the resonance at critical coupling (1538.71 nm). The ΔT_{Ring} for different voltages is normalized with respect to the IL, measured at an initial bias voltage of 6 V. One can confirm from

the T_{Ring} spectra of device I in the bottom right inset of figure 2a, that the ring is initially in the under-coupled regime at 0 V. As we increase the applied voltage to 8 V, the resonator becomes critically-coupled and at voltages exceeding 10 V, the ring becomes over-coupled with a strong blue detuning of the resonance wavelength (for detailed results, see Supplementary section III).

We measure a 3 dB electro-optic bandwidth of 14.9 ± 0.1 GHz in the composite SiN-2D waveguide. In figure 2b, we show the frequency response of device I, which we measure using a 70 GHz fast photodiode and an electrical vector network analyzer (VNA) at 1569.6 nm for a bias voltage of 8 V with a RF voltage swing of 10 dBm. One can see from the measured T_{Ring} at 1569.6 nm in the inset of figure 2b, that the optical bandwidth supported by the device at 8 V is 15.8 GHz ($Q_L \sim 12000$). We ensure that the optical bandwidth supported by the device at 8 V is higher than the measured electro-optic bandwidth (14.9 GHz) that is currently limited by the contact resistance of monolayer Gr and WSe₂ (see supplementary section IV).

We show that the voltage dependent phase and transmission change in ring resonators can be tailored with the device geometry. We engineer the length of Gr-Al₂O₃-WSe₂ capacitor to achieve a similar phase change of $(0.50 \pm 0.05) \pi$ radians as observed in device I, while ensuring a comparatively lower IL of 2.96 ± 0.34 dB and low ΔT_{Ring} of 1.73 ± 0.20 dB. The optimized device (hereafter, referred to as device II) consists of a 25 μm -long Gr-Al₂O₃-WSe₂ capacitor embedded in the SiN ring, with a ring-bus gap of 450 nm. The shorter capacitor exhibits lower pin-hole defects that results in an increase of the breakdown voltage from 22 V in device I to 30 V in device II. The high breakdown fields enable a higher degree of transparency in SiN waveguide, thereby

facilitating strong tuning of the coupling regime (see Supplementary section V). Similar to the configuration of device I, the ring achieves critical coupling with a Q_L of $\sim 18,730$ at 8.5 V. We probe the $\Delta\varphi_T$ (top panel of figure 2a) and ΔT_{Ring} (bottom panel of figure 2a) at a λ_p , that is blue detuned by 0.04 nm with respect to the resonance wavelength at critical coupling (1646.22 nm). The $\Delta\varphi_T$ of the ring are extracted from the measured T_{Ring} for different voltages applied across the capacitor (see Supplementary section VI). We further confirm that the $\Delta\varphi_T$ extracted from the T_{Ring} is in strong agreement with the $\Delta\varphi_T$ measured using an external Mach-Zehnder interferometer (MZI) configuration (often used for phase measurements)^{38,39,31}. We measure $\Delta\varphi_T$ by simultaneously probing both the T_{Ring} , and the transmission at the output of an MZI (T_{MZI}) when device I is embedded in one of the arms of a fiber-based MZI. Supplementary section VII details the experimental setup used for measuring the phase response of our devices, while supplementary section VIII shows the measured T_{Ring} and T_{MZI} at the output of the ring resonator, for different voltages applied across the Gr-Al₂O₃-WSe₂ capacitor.

We verify that the ratio between the Δn_{eff} and Δk_{eff} of the composite SiN-2D waveguide is close to unity. Figure 3a shows the measured Δn_{eff} and Δk_{eff} of the ring, which is extracted from the measured T_{Ring} for various voltages applied across the 25 μm long Gr-Al₂O₃-WSe₂ capacitor in device II (see Supplementary section IX). One can see that the Δk_{eff} decreases progressively with an increase in the gate voltage and Δn_{eff} shows an initial increase leading to a red-shift in the resonance wavelength, followed by a strong decrease which leads to a strong blue detuning. The maximum Δn_{eff} and Δk_{eff} for an applied voltage of 30 V is -6.0×10^{-4} RIU and -7.8×10^{-4} RIU respectively, which corresponds to a $\frac{\Delta n_{eff}}{\Delta k_{eff}} \sim 0.78$.

We extract the contribution of the electro-optic response of each of the 2D layers to the Δn_{eff} and Δk_{eff} , by modeling the monolayers as a hybrid 2D sheet integrated on a SiN waveguide using finite element model (see Methods and Supplementary Section X). Figure 3b shows the change in the normalized imaginary and real part of the optical conductivity of monolayer graphene $\left(\frac{\sigma_G}{\sigma_0}\right)$ that imparts a proportional change in the Δn_{eff} and Δk_{eff} of the propagating mode, respectively. From the modeling of the Gr monolayer, we find that the Gr is initially p-doped with $(5.20 \pm 0.30) \times 10^{12} \text{ cm}^{-2}$ carriers (i.e. $E_{F_{\text{init}}} = 0.240 \pm 0.006 \text{ eV}$) and becomes completely transparent at voltages exceeding 25 V. Figure 3c shows the change in the real and imaginary part of the refractive index of WSe₂ (Δn_{WSe_2} and Δk_{WSe_2}) as a function of the applied voltage. For a maximum electron doping of $(2.54 \pm 0.74) \times 10^{13} \text{ cm}^{-2}$ at 30 V, the Δn_{WSe_2} reaches $-0.69 \pm 0.05 \text{ RIU}$, while Δk_{WSe_2} (which induces insertion loss) remains below $0.010 \pm 0.002 \text{ RIU}$.

We measure a phase modulation efficiency ($V_{\pi/2} \cdot L_{\pi/2}$) of $0.045 \text{ V} \cdot \text{cm}$ with an insertion loss ($\text{IL}_{\pi/2}$) of 4.7 dB for a phase change of $\pi/2$ radians. We show in figure 4 and Supplementary section XI, that device II performs with a significantly lower $V_{\pi/2} \cdot L_{\pi/2}$ (i.e., enhanced phase modulation efficiency) and lower $\text{IL}_{\pi/2}$, when compared to the existing phase modulation technologies. We find that the $V_{\pi/2} \cdot L_{\pi/2}$ for our SiN-2D hybrid platform is at least an order of magnitude lower than the one of electro-refractive phase modulators based on dielectric materials such as silicon PN, PIN and MOS capacitors^{1,3,7,9-11}, III-V on silicon²², graphene on silicon modulators¹⁸ and lithium niobate (LN) devices^{16,17}, and can be achieved with a relatively low $\text{IL}_{\pi/2}$. In figure 4, we show a comparison with current state-of-art phase modulation technologies. One can see that by overcoming the traditional tradeoff between propagation length and insertion loss through

simultaneous index and loss modulation in ring resonators, our SiN-2D platform facilitates the development of compact phase modulators with low $V_{\pi/2} \cdot L_{\pi/2}$ and minimal optical loss.

The SiN-2D hybrid platform enables the design of compact and highly reconfigurable photonic circuits with tunable coupling and the ability to achieve phase modulation at several gigahertz of electro-optic bandwidth. We show a novel paradigm of designing efficient and compact phase modulators by leveraging cavities embedded with a hybrid material that has a $\frac{\Delta n}{\Delta k}$ close to unity. Alternately, one can realize high-speed intensity modulation with low insertion loss using the same SiN-2D platform, by probing the response at the resonance wavelength^{40,41}. The potential of our SiN-2D platform to become transparent with doping and the ability to modify the coupling in cavities at several gigahertz of electro-optic bandwidth enables its use in various applications such as optical memories, frequency combs and optical communication systems⁴¹.

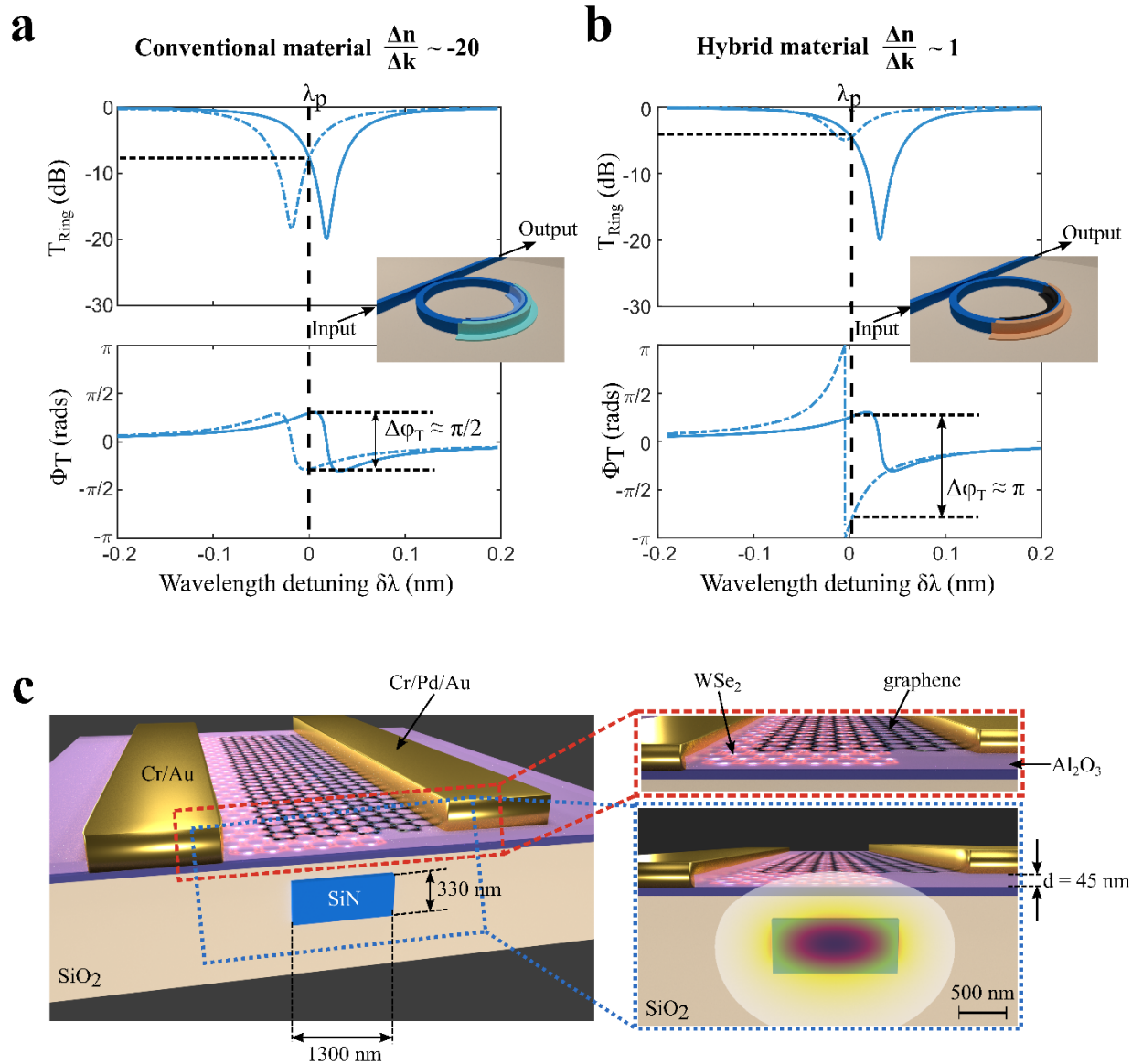


Figure 1 | Illustration of SiN-2D platform leveraging loss and index change for phase modulation. (a) Normalized transmission (T_{Ring}) and phase response (ϕ_T) of a ring resonator embedded with a conventional material that undergoes a strong change in index i.e. $\frac{\Delta n}{\Delta k} \sim -20$. The inset shows the schematic of a ring resonator with a portion ($\sim 8\%$) of the ring covered with the active conventional material. For a ring operating near the critically-coupled regime with a loaded quality factor (Q_L) of ~ 20000 , the Δn of -6×10^{-4} RIU induces a blue shift in the resonance wavelength of the ring response. At a probe wavelength of λ_p , the cavity experiences a strong phase change that is accompanied with a prohibitively high insertion loss. (b) T_{Ring} and ϕ_T of a ring resonator embedded with a hybrid material that undergoes simultaneous index and loss change i.e. $\frac{\Delta n}{\Delta k} \sim 1$. For a similar ring with $\sim 8\%$ of the ring

covered with the hybrid material, with the ring Q_L of ~ 20000 and a Δn of -6×10^{-4} RIU, one can observe a strong blue shift in the resonance wavelength with drastic change in the coupling regime. When probed at λ_p , one can achieve a strong phase change at of $\sim \pi$ radians with an insertion loss as low as 4.5 dB. (c) Illustration of a composite SiN-2D hybrid platform with monolayer Gr and WSe₂ to tune the loss and index of SiN waveguide, respectively. Device cross-section showing Gr-Al₂O₃-WSe₂ capacitor, embedded on a 1300 nm wide \times 330 nm high SiN waveguide. Top right inset shows the Gr-Al₂O₃-WSe₂ parallel plate capacitor configuration which electrostatically gates both the monolayers by applying a voltage across the dielectric. Bottom right inset indicates the position of the monolayer Gr and WSe₂ in the mode-profile of the SiN waveguide.

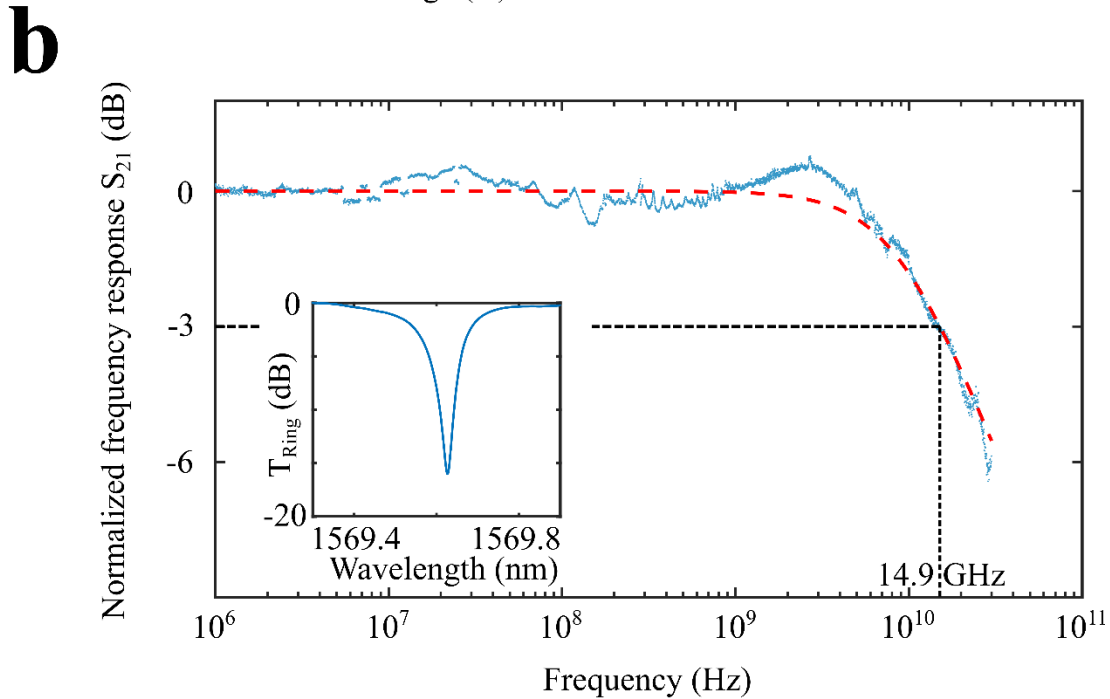
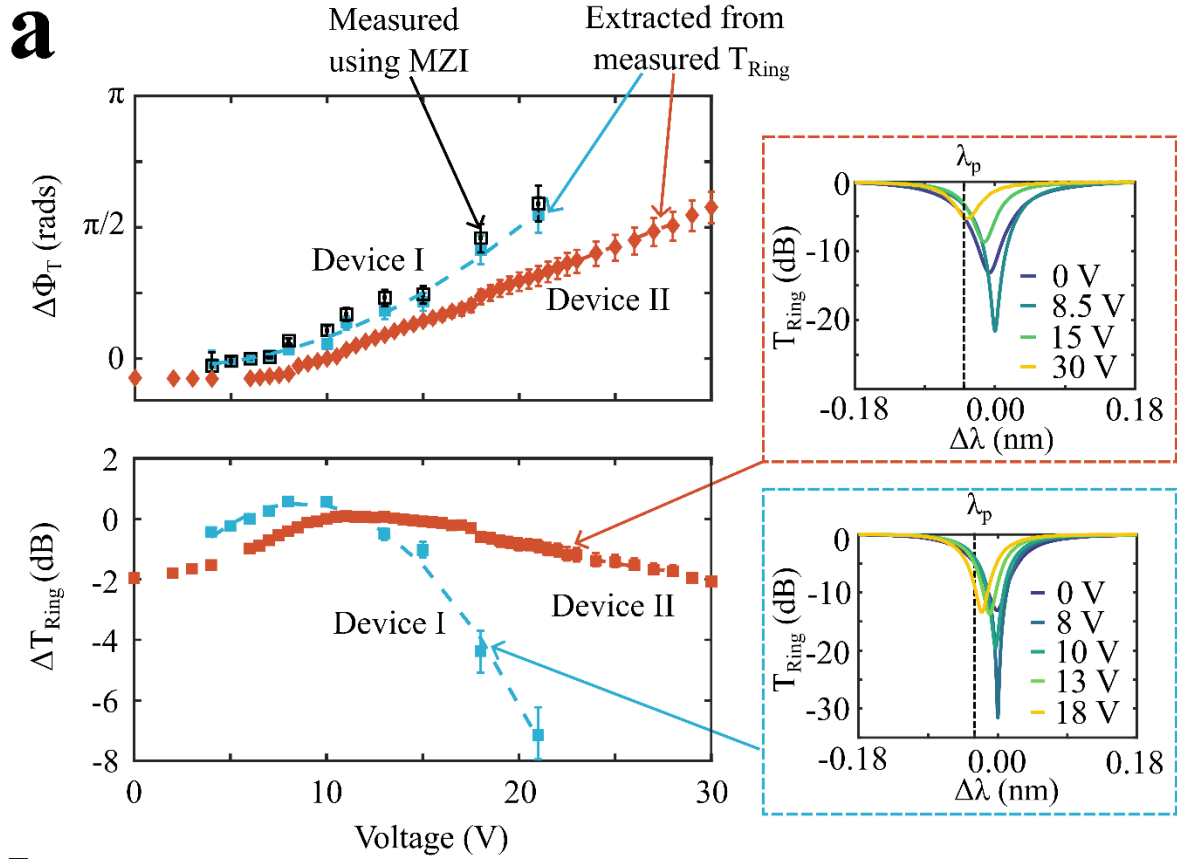


Figure 2: Phase measurement and electro-optic bandwidth of SiN-2D hybrid waveguide embedded in a SiN ring resonator. (a) Phase change ($\Delta\phi_T$ in radians) in the top panel and transmission modulation (ΔT_{Ring} in dB) in the

bottom panel at probe wavelength detuning (λ_p), for different voltages applied across two Gr-Al₂O₃-WSe₂ capacitors embedded in a SiN ring resonator of 50 μm radius. The blue markers show the extracted $\Delta\phi_T$ and measured ΔT_{Ring} for device I. One can see a continuous phase change ($\Delta\phi_T$) of $(0.46 \pm 0.05) \pi$ radians in device I with an insertion loss (IL) of 4.78 ± 0.40 dB and ΔT_{Ring} of 4.37 ± 0.70 dB for an applied voltage swing from 6 V to 18 V. The orange markers show the extracted $\Delta\phi_T$ and measured ΔT_{Ring} for device II. One can see that the device II can enable a $\Delta\phi_T$ of $(0.50 \pm 0.05) \pi$ radians with a comparatively lower IL of 2.96 ± 0.34 dB and lower ΔT_{Ring} of 1.73 ± 0.20 dB. The T_{Ring} spectra for device I and II shows that the rings are initially in the under-coupled regime at 0 V, becomes critically-coupled at 8.5 V and enters the over-coupled regime at voltages exceeding 10 V. We further confirm using device I, that the $\Delta\phi_T$ extracted from the T_{Ring} correlates strongly with the $\Delta\phi_T$ measured using a Mach-Zehnder interferometer (MZI) configuration (see black markers). (b) Normalized frequency response (S_{21}) of device I at 1569.6 nm for a bias voltage at 8 V.

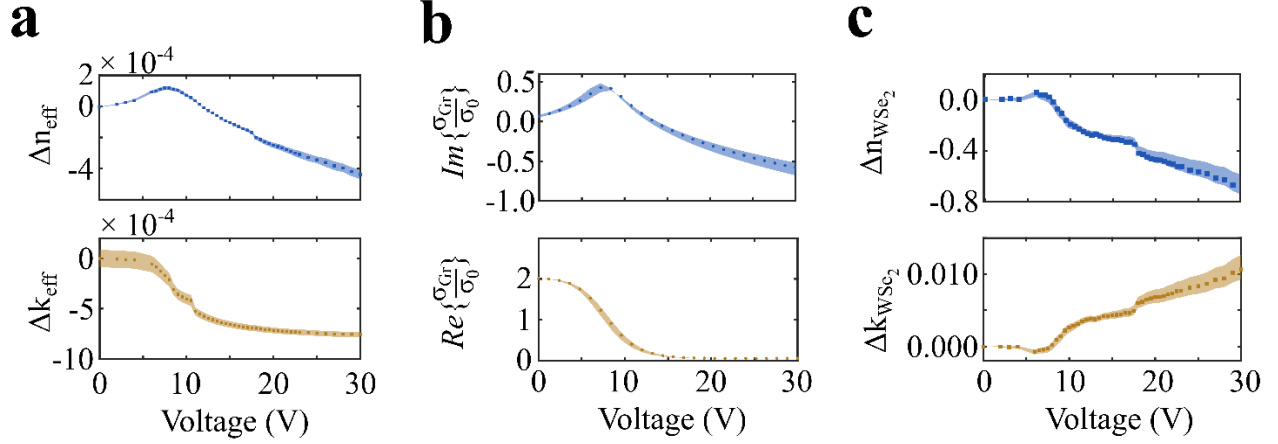


Figure 3: Change in complex effective index of the mode and relative contribution of the Gr and WSe₂ monolayers. (a) Change in the real (top) and imaginary (bottom) part of the effective index (Δn_{eff} and Δk_{eff} in refractive index units (RIU)) of the composite SiN-2D waveguide at different voltages, extracted from the normalized T_{Ring} of device II. The shaded area represents the root-mean-square (r.m.s.) error from the numerical fit³³ (see Supplementary section X). (b) Change in the imaginary (top) and real (bottom) part of the normalized optical conductivity of monolayer graphene ($\frac{\sigma_G}{\sigma_0}$) that imparts a proportional change in the Δn_{eff} and Δk_{eff} of the propagating mode, respectively. The shaded area includes the r.m.s error in the effective index and the error in the extracted initial doping of monolayer graphene, dielectric permittivity of Al₂O₃ and the variation in the height of the SiO₂ cladding separating the capacitive stack from the SiN waveguide (180 ± 10 nm). (c) Change in the real (top) and imaginary (bottom) part of the refractive index of monolayer WSe₂ (Δn_{WSe_2} and Δk_{WSe_2} in RIU) with voltage. The shaded region incorporates the r.m.s error in the complex effective index, error in the ($\frac{\sigma_G}{\sigma_0}$) of graphene and a ± 0.05 nm variation in the thickness of the monolayer WSe₂ ($h_{\text{WSe}_2} \sim 0.65$ nm)^{42,43}.

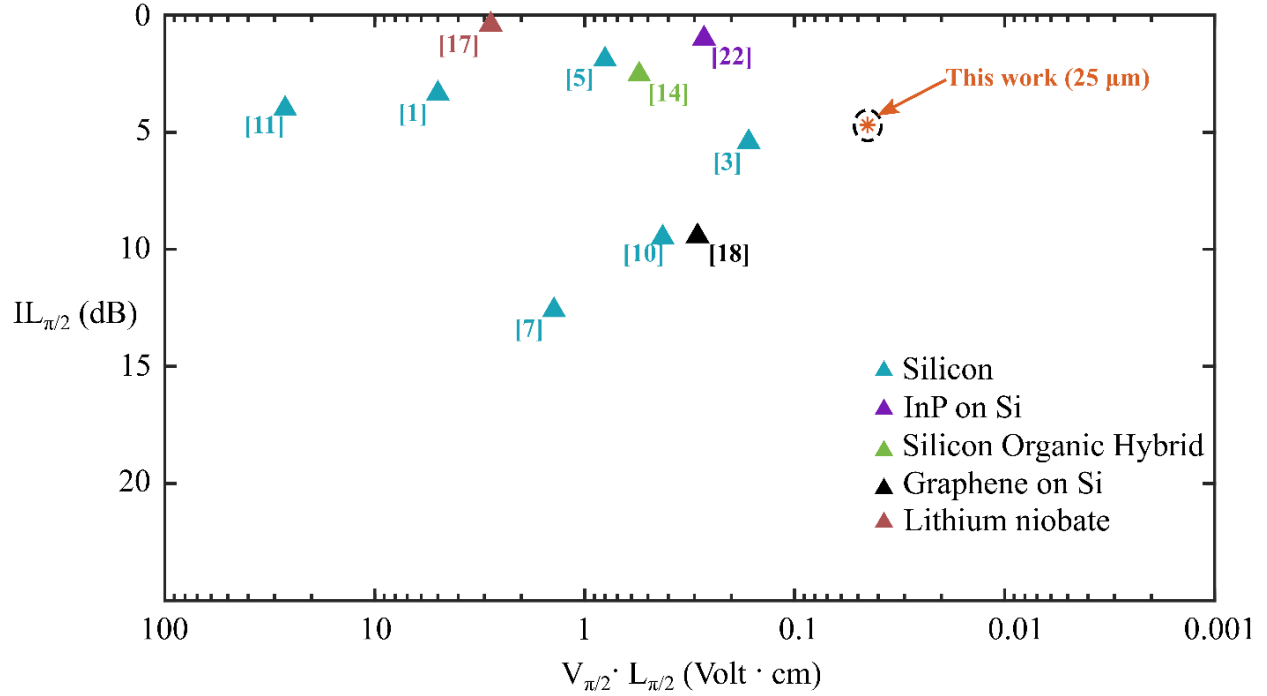


Figure 4: Comparison of insertion loss ($IL_{\pi/2}$) vs. phase modulation efficiency (i.e. voltage length product ($V_{\pi/2} \cdot L_{\pi/2}$)) for various electro-optic phase modulators. We show that the $V_{\pi/2} \cdot L_{\pi/2}$ of our device II (0.045 V · cm) is at least an order of magnitude lower than conventional electro-refractive phase modulators based on silicon^{1,3,5,7,10,11}, III-V materials such as InP on silicon²², graphene on silicon¹⁸, slot-based silicon-organic hybrid material¹⁴. Low-loss phase modulation can be achieved by using LN devices^{16,17}, which comes at the expense of a $V_{\pi/2} \cdot L_{\pi/2}$ that is almost two-orders of magnitude higher than our device.

References

1. Liu, A. *et al.* A high-speed silicon optical modulator based on a metal–oxide–semiconductor capacitor. *Nature* **427**, 615–618 (2004).
2. Liao, L. *et al.* High speed silicon Mach-Zehnder modulator. *Opt. Express* **13**, 3129–3135 (2005).
3. Green, W. M. J., Rooks, M. J., Sekaric, L. & Vlasov, Y. A. Ultra-compact, low RF power, 10 Gb/s silicon Mach-Zehnder modulator. *Opt. Express* **15**, 17106–17113 (2007).
4. Chen, H.-W., Kuo, Y. & Bowers, J. E. High speed hybrid silicon evanescent Mach-Zehnder modulator and switch. *Opt. Express* **16**, 20571–20576 (2008).
5. Feng, N.-N. *et al.* High speed carrier-depletion modulators with 1.4V-cm $V_{\pi}L$ integrated on 0.25 μm silicon-on-insulator waveguides. *Opt. Express* **18**, 7994–7999 (2010).
6. Reed, G. T., Mashanovich, G., Gardes, F. Y. & Thomson, D. J. Silicon optical modulators. *Nat. Photonics* **4**, 518–526 (2010).
7. Thomson, D. J. *et al.* High contrast 40Gbit/s optical modulation in silicon. *Opt. Express* **19**, 11507–11516 (2011).
8. Ziebell, M. *et al.* 40 Gbit/s low-loss silicon optical modulator based on a p-i-n diode. *Opt. Express* **20**, 10591–10596 (2012).
9. Baehr-Jones, T. *et al.* Ultralow drive voltage silicon traveling-wave modulator. *Opt. Express* **20**, 12014–12020 (2012).
10. Brimont, A. *et al.* High-contrast 40 Gb/s operation of a 500- μm long silicon carrier-depletion slow wave modulator. *Opt. Lett.* **37**, 3504–3506 (2012).
11. Tu, X. *et al.* 50-Gb/s silicon optical modulator with traveling-wave electrodes. *Opt. Express* **21**, 12776–12782 (2013).

12. Reed, G. T. *et al.* Recent breakthroughs in carrier depletion based silicon optical modulators. *Nanophotonics* **3**, 229–245 (2013).
13. Xiao, X. *et al.* High-speed, low-loss silicon Mach–Zehnder modulators with doping optimization. *Opt. Express* **21**, 4116–4125 (2013).
14. Alloatti, L. *et al.* 100 GHz silicon–organic hybrid modulator. *Light Sci. Appl.* **3**, e173–e173 (2014).
15. Abraham, A., Olivier, S., Marris-Morini, D. & Vivien, L. Evaluation of the performances of a silicon optical modulator based on a silicon-oxide-silicon capacitor. in *11th International Conference on Group IV Photonics (GFP)* 3–4 (2014). doi:10.1109/Group4.2014.6961999.
16. Wang, C., Zhang, M., Stern, B., Lipson, M. & Lončar, M. Nanophotonic lithium niobate electro-optic modulators. *Opt. Express* **26**, 1547–1555 (2018).
17. Wang, C. *et al.* Integrated lithium niobate electro-optic modulators operating at CMOS-compatible voltages. *Nature* **562**, 101 (2018).
18. Soriano, V. *et al.* Graphene–silicon phase modulators with gigahertz bandwidth. *Nat. Photonics* **12**, 40–44 (2018).
19. Kieninger, C. *et al.* Ultra-high electro-optic activity demonstrated in a silicon-organic hybrid modulator. *Optica* **5**, 739–748 (2018).
20. Hiraki, T. *et al.* Heterogeneously integrated III–V/Si MOS capacitor Mach–Zehnder modulator. *Nat. Photonics* **11**, 482–485 (2017).
21. Han, J.-H. *et al.* Efficient low-loss InGaAsP/Si hybrid MOS optical modulator. *Nat. Photonics* **11**, 486–490 (2017).
22. Ogiso, Y. *et al.* Over 67 GHz Bandwidth and 1.5 V $V\pi$ InP-Based Optical IQ Modulator With n-i-p-n Heterostructure. *J. Light. Technol.* **35**, 1450–1455 (2017).

23. Weigel, P. O. *et al.* Bonded thin film lithium niobate modulator on a silicon photonics platform exceeding 100 GHz 3-dB electrical modulation bandwidth. *Opt. Express* **26**, 23728–23739 (2018).
24. He, M. *et al.* High-performance hybrid silicon and lithium niobate Mach–Zehnder modulators for 100 Gbit s⁻¹ and beyond. *Nat. Photonics* **13**, 359–364 (2019).
25. Xu, M. *et al.* High-performance coherent optical modulators based on thin-film lithium niobate platform. *Nat. Commun.* **11**, 3911 (2020).
26. Xu, Q., Schmidt, B., Pradhan, S. & Lipson, M. Micrometre-scale silicon electro-optic modulator. *Nature* **435**, 325–327 (2005).
27. Chen, L., Xu, Q., Wood, M. G. & Reano, R. M. Hybrid silicon and lithium niobate electro-optical ring modulator. *Optica* **1**, 112–118 (2014).
28. Xu, Q., Manipatruni, S., Schmidt, B., Shakya, J. & Lipson, M. 12.5 Gbit/s carrier-injection-based silicon micro-ring silicon modulators. *Opt. Express* **15**, 430–436 (2007).
29. Preble, S. F., Xu, Q. & Lipson, M. Changing the colour of light in a silicon resonator. *Nat. Photonics* **1**, 293–296 (2007).
30. Xu, Q., Dong, P. & Lipson, M. Breaking the delay-bandwidth limit in a photonic structure. *Nat. Phys.* **3**, 406–410 (2007).
31. Liang, G. *et al.* Efficient Pure Phase Optical Modulator Based on Strongly Over-Coupled Resonators. in *Conference on Lasers and Electro-Optics (2019)*, paper STh3H.1 STh3H.1 (Optical Society of America, 2019). doi:10.1364/CLEO_SI.2019.STh3H.1.
32. Larocque, H. *et al.* Beam steering with ultracompact and low-power silicon resonator phase shifters. *Opt. Express* **27**, 34639–34654 (2019).

33. Manolatou, C. *et al.* Coupling of modes analysis of resonant channel add-drop filters. *IEEE J. Quantum Electron.* **35**, 1322–1331 (1999).
34. Wang, F. *et al.* Gate-Variable Optical Transitions in Graphene. *Science* **320**, 206–209 (2008).
35. Liu, M. *et al.* A graphene-based broadband optical modulator. *Nature* **474**, 64–67 (2011).
36. Phare, C. T., Lee, Y.-H. D., Cardenas, J. & Lipson, M. Graphene electro-optic modulator with 30 GHz bandwidth. *Nat. Photonics* **9**, 511–514 (2015).
37. Datta, I. *et al.* Low-loss composite photonic platform based on 2D semiconductor monolayers. *Nat. Photonics* **14**, 256–262 (2020).
38. Cardenas, J. *et al.* Linearized silicon modulator based on a ring assisted Mach Zehnder interferometer. *Opt. Express* **21**, 22549–22557 (2013).
39. Aldaya, I., Gil-Molina, A., Fragnito, H. L. & Dainese, P. Time-domain interferometric characterization of nonlinear and thermal-induced phase-shift in silicon waveguides. in *2016 Conference on Lasers and Electro-Optics (CLEO)* 1–2 (2016).
40. Datta, I. *et al.* Platform for ultra-strong modulation in hybrid silicon nitride/2D material photonic structures. in *Conference on Lasers and Electro-Optics (2020)*, paper SF2J.4 SF2J.4 (Optical Society of America, 2020). doi:10.1364/CLEO_SI.2020.SF2J.4.
41. Datta, I., Gordillo, O. A. J., Chae, S. H., Hone, J. & Lipson, M. Platform for electrically reconfigurable ring resonator based on TMD-graphene composite waveguides. in *Conference on Lasers and Electro-Optics (2021)*, paper STh5B.1 STh5B.1 (Optica Publishing Group, 2021). doi:10.1364/CLEO_SI.2021.STh5B.1.
42. Fang, H. *et al.* High-Performance Single Layered WSe₂ p-FETs with Chemically Doped Contacts. *Nano Lett.* **12**, 3788–3792 (2012).

43. Li, Z. *et al.* Layer Control of WSe₂ via Selective Surface Layer Oxidation. *ACS Nano* **10**, 6836–6842 (2016).
44. Liu, F. *et al.* Disassembling 2D van der Waals crystals into macroscopic monolayers and reassembling into artificial lattices. *Science* **367**, 903–906 (2020).
45. Zhu, Y. *et al.* Monolayer Molybdenum Disulfide Transistors with Single-Atom-Thick Gates. *Nano Lett.* (2018) doi:10.1021/acs.nanolett.8b01091.
46. Ji, X. *et al.* Ultra-low-loss on-chip resonators with sub-milliwatt parametric oscillation threshold. *Optica* **4**, 619–624 (2017).

Acknowledgement

Research on tunable electro-optic phenomenon in TMD semiconductors and graphene monolayers was supported as part of Energy Frontier Research Center (EFRC) on Programmable Quantum Materials funded by the U.S. Department of Energy (DOE), Office of Science, Basic Energy Sciences (BES), under award #DE-SC0019443. Research of I.D. on leveraging 2D materials for low-loss phase shifters was funded by Defense Advance Projects Agency (DARPA) award no. #FA8650-16-7643 and the Air Force Office of Scientific Research (AFOSR) MURI award no. N00014-16-1-2219. The platform development was partially supported by the Co-design Center for Quantum Advantage (C2QA – BNL No.390033). This work was done in part at the City University of New York Advanced Science Research Facility. We acknowledge the use of facilities and instrumentation supported by NSF through the Columbia University, Columbia Nano Initiative, and the Materials Research Science and Engineering Center DMR-2011738. We thank Dr. Brian S. Lee for his guidance with the improved graphene transfer and Dr. Gaurang R. Bhatt, Dr. Janderson Rocha Rodrigues, Dr. Utsav Deepak Dave and Dr. Aseema Mohanty for fruitful discussions.

Contributions

I.D. and M.L. conceived and proposed the SiN-2D photonic design and experiments. I. D. fabricated the composite SiN-2D photonic device with assistance from S. H. C. for TMD transfer. I. D. performed and analyzed the optical experiments, with assistance from A. G. M. regarding the external fiber-based MZI setup for measuring phase in ring resonators. I. D. and M. L. prepared the manuscript. A. G. M., S. H. C., J. H. and M. L. edited the manuscript. M. L. supervised the project.

Methods

WSe₂ transfer and patterning

We leverage the facile method described in Ref ⁴⁴ to exfoliate large-area monolayer WSe₂ onto our SiN waveguides, covered with 180 nm of planarized SiO₂. We start with an atomically flat gold film, deposited by evaporating 150 nm thin Au films onto an ultra-flat surface of highly polished silicon wafer, where the gold film is stripped away off the substrate using a combination of the thermal release tape with a polyvinylpyrrolidone (PVP) interfacial layer. The ultra-flat gold tape allows for a uniform contact between the gold and monolayer WSe₂ crystal surface (HQ Graphene- <http://www.hqgraphene.com/WSe2.php>), exfoliating a complete monolayer that can be transferred onto our planarized SiN waveguides. We remove the thermal release tape by heating our substrate to 100 °C, washing off the PVP layer and etching the gold with a mild solution of gold etchant (I₂/I⁻). Supplementary figure S21 shows the extent of the coverage of monolayer WSe₂ after the gold assisted transfer of WSe₂ onto our planarized SiN substrates. Supplementary figure S22 shows the photoluminescence (PL) spectrum of as transferred monolayer WSe₂ on our SiO₂ covered SiN substrate using a Renishaw InVia Micro-Raman spectrometer at an excitation wavelength of 532 nm.

We pattern a 50 μm long WSe₂ monolayer by spinning a dual resist mask of 400 nm/120 nm PMMA/HSQ (XR-1561 6%) film, followed by baking the pattern at 180 °C for 15 mins (PMMA)/4 mins (HSQ), respectively, patterning using EBL and reactive ion etching (RIE) based O₂ plasma

treatment for 4 min 30 secs to etch the residual PMMA and monolayer WSe₂. After the etch, we strip the resist in acetone, where it dissolves the PMMA, cleanly removing the HSQ mask.

Graphene transfer and patterning

We use chemical vapor deposited (CVD) graphene grown on 3-inch × 3-inch copper films (Grolltex - <https://grolltex.com/>). We prepare the graphene samples for transfer by first spinning PMMA 495 A6 at 1000 rpm and drying the 500 nm PMMA coated graphene on Cu film overnight in ambient conditions. We electrochemically delaminate the PMMA/graphene stack from the Cu film using the process described in Ref⁴⁵. We prepare 1M NaOH aqueous solution as an electrolyte and delaminate the PMMA/Gr stack by using the PMMA/Gr on Cu foil as the cathode, and a bare Cu foil as the anode. The delaminated PMMA/Gr stack is then transferred to a fresh water bath and this process is repeated a few times, before being transferred onto the SiN substrate. We enhance the hydrophilicity of the substrate and remove moisture/polymer contamination by performing O₂ plasma clean on the sample for 30 minutes prior to the transfer. Following the transfer, we vacuum dry the as transferred sample overnight in a vacuum desiccator, followed by baking the sample at 180 °C for 2 hours. Finally, the PMMA is dissolved away in acetone solution by submerging the chip in acetone for about 4 hours. Supplementary figure S23 shows the Raman spectra of the top graphene sheet after the transfer.

We pattern a 25 μm / 40 μm long graphene monolayer by spinning a composite resist mask of 400 nm/120 nm PMMA/HSQ (XR-1561 6%) film, followed by baking the pattern at 180 °C for 15 mins (PMMA)/4 mins (HSQ), respectively, patterning using EBL and reactive ion etching (RIE) based O₂ plasma treatment for 1 min 30 secs to etch the residual PMMA and graphene. After the etch, we strip the resist in acetone, where it dissolves the PMMA, cleanly removing the HSQ mask.

Device fabrication for Gr-Al₂O₃-WSe₂ based capacitive SiN photonic device

We lithographically defined 1.3 μm wide waveguides on 330 nm high silicon nitride (SiN), deposited using Low Pressure Chemical Vapor Deposition (LPCVD) at 800 °C and annealed at 1200 °C for 3 hours on 4.2 μm thermally oxidized SiO₂, using a combination of deep ultraviolet (DUV) lithography to define the chemical planarization (CMP) pillars of 5 μm length × 5 μm

width, with 33 % fill factor in the wafer area, surrounding the waveguides and ebeam lithography (EBL) to define the waveguides. In order to obtain low-loss SiN waveguides at near infrared (NIR) wavelengths, we leverage an optimized etch recipe, described in Ref ⁴⁶ to reduce the surface roughness of SiN waveguides that contributes to the propagation loss in low confinement SiN waveguides. We etch the SiN waveguides and CMP patterns using an optimized CHF₃/O₂ recipe with increased oxygen flow to reduce *in situ* polymer formation in Oxford 100 Plasma ICP RIE, using 360 nm of PECVD SiO₂ as a hard mask for etching the SiN thin film. We remove the residual SiO₂ hard mask using a 100:1 buffered oxide etch solution (BOE) to reduce the roughness due to etch, followed by deposition of 600 nm of Plasma Enhanced Chemical Vapor Deposition (PECVD) silicon dioxide (SiO₂) on the waveguides for planarization. We planarize the SiO₂ to 180 nm ± 15 nm above the SiN waveguides using standard CMP techniques to create a planar surface for the transfer of monolayer TMD such as WSe₂ and to prevent the WSe₂ film from breaking at the waveguide edges. We clean the planarized surface with Piranha solution at 100 C to remove the slurry particles that settle during CMP process. The 180 nm SiO₂ layer additionally aids in reducing the optical propagation loss introduced by the interaction of the undoped graphene monolayer with the optical mode. A 15 nm of sacrificial thermal atomic layer-deposited (ALD) alumina (Al₂O₃) is deposited on top of SiO₂ to isolate the SiN waveguides from the subsequent fabrication steps required for the patterning of monolayer TMDs. Following the WSe₂ transfer and patterning steps described above, the metal contacts are lithographically patterned using EBL, and 0.5 nm/30 nm/80 nm of Cr/Pd/Au was deposited using electron-beam evaporation, followed by liftoff in acetone. The metal contacts to WSe₂ monolayer are placed at a distance of 1.5 μm away from the SiN waveguide, in order to reduce the propagation loss and minimize sheet resistance. A 10 nm/35 nm (100 loops/ 375 loops) layer of thermal ALD Al₂O₃ at 200 °/270 °C is then deposited to form the dielectric of the Gr-Al₂O₃-WSe₂ capacitor. In order to reduce the metal-WSe₂ contact resistance, we anneal the SiN waveguide with Al₂O₃ covered WSe₂ at 270 °C for 4 hours in vacuum. We then transfer and pattern monolayer graphene, as described in the section above, followed by vacuum annealing the composite Gr-Al₂O₃-WSe₂ on SiN waveguide at 275 °C for 4 hours in vacuum to remove PMMA residue left on graphene monolayer after the transfer and patterning. Following this, the metal contacts to the graphene layer is patterned using EBL and 5 nm/20 nm/50 nm of Cr/Pd/Au is then deposited using electron-beam evaporation, followed by liftoff in acetone. Similar to the metal placement configuration on WSe₂ monolayers, the metal

contacts are placed at an offset of 1.5 μm from the SiN waveguide. Finally, we define and wet etch (100:1 BOE) the vias to open the metal electrodes in contact with WSe₂, for testing. We achieve high electro-optic bandwidth in our devices by optimizing the graphene transfer process, involving multiple annealing steps in our device fabrication, depositing a 45 nm thick dielectric that minimizes pin-hole defects and finally optimizing the metal contacts to both the monolayer to reduce the contact resistance.

Optical sheet conductivity of monolayer WSe₂ and graphene

We use the 2D sheet conductivity model to extract the electro-optic response of monolayer Gr and monolayer semiconductor WSe₂, as is commonly done when modelling graphene monolayers. The change in real part of the effective index of the composite SiN-2D waveguide (Δn_{eff}) in the top panel of figure 3a is a combination of the electro-refractive response of graphene i.e. $Im \left\{ \frac{\sigma_G}{\sigma_0} \right\}$ and monolayer WSe₂ (Δn_{WSe_2}). We predominantly attribute the change in the imaginary part of the effective index (Δk_{eff}) in the bottom panel of figure 3a, to the change in real part of the normalized complex conductivity i.e. $Re \left\{ \frac{\sigma_G}{\sigma_0} \right\}$ of graphene with voltage. In accordance with the relation in equation (1), the $Re \left\{ \frac{\sigma_G}{\sigma_0} \right\}$ is related to the imaginary part of dielectric permittivity, that contributes to absorption, whereas the $Im \left\{ \frac{\sigma_G}{\sigma_0} \right\}$ is related to the real part of dielectric permittivity, that contributes to the change in index of monolayer graphene.

$$\sigma_G(\omega) = j\omega t_d \epsilon_0 (\epsilon(\omega) - 1) \quad (1)$$

Since the electro-optic response of graphene predominantly affects the Δk_{eff} , we extract the normalized sheet conductivity of monolayer graphene as a function of applied voltage, by comparing the measured Δk_{eff} in our experiments to the simulated change obtained using COMSOL Multiphysics finite element model. We model the monolayer graphene as a conductive sheet, with surface charge density ($J = \sigma_G(\omega) \cdot E$), with conductivity given by equation (3). The optical properties of graphene can be tuned by doping graphene electrostatically[47], [48] i.e. by applying a voltage across the Gr-Al₂O₃-WSe₂ capacitor. The doping of graphene induces a shift in the fermi energy level of graphene (E_F), given by

$$E_F = \hbar v_F \sqrt{\left(\pi \left(\frac{\varepsilon_0 \varepsilon_R V}{de} + n_{initial} \right) \right)} \quad (2)$$

where, ε_0 is the vacuum permittivity, ε_R is the relative permittivity of the dielectric Al_2O_3 separating the two monolayers, e is the electronic charge, v_F is the fermi velocity in graphene, and $n_{initial}$ is the initial chemical doping of the graphene layer (which is dependent on the processing of graphene and on the substrate). The normalized optical conductivity of graphene ($\frac{\sigma_G}{\sigma_0}$) is related to the fermi level through the following equation

$$\frac{\sigma_G(\omega)}{\sigma_0} = \frac{1}{2} \left(\tanh\left(\frac{\hbar\omega + 2E_F}{4k_B T}\right) + \tanh\left(\frac{\hbar\omega - 2E_F}{4k_B T}\right) - \frac{i}{\pi} \left(\log\left(\frac{(\hbar\omega + 2E_F)^2}{(\hbar\omega - 2E_F)^2 + (2k_B T)^2}\right) \right) + \frac{i8}{\pi} \left(\frac{E_F}{\hbar\omega + i\hbar\gamma} \right) \right) \quad (3)$$

where σ_0 is the universal conductivity of graphene, \hbar is the reduced Planck's constant, ω is the optical frequency, k_B is the Boltzmann constant, T is the temperature and γ is the intra-band carrier relaxation rate, assumed to be 100 fs, as predicted for similar structures. We find from our simulations that the graphene is initially p-doped with $(5.2 \pm 0.3) \times 10^{12} \text{ cm}^{-2}$ carriers ($E_{\text{Finit}} = 0.24 \pm 0.006 \text{ eV}$) and the slope of Δk_{eff} indicates that the $\varepsilon_r = 6.9 \pm 0.2$. We model monolayer WSe_2 , similar to graphene and is explained in detail in Ref [39]. We extract a change of $\sim 18\%$ in the refractive index of monolayer WSe_2 with an electron doping density of $(2.54 \pm 0.74) \times 10^{13} \text{ cm}^{-2}$ at 30 V.